Defect segregation facilitates oxygen transport at fluorite UO_2 grain boundaries

A. R. Symington[1], M. Molinari[2], N. A. Brincat[3], N. R.Williams[3] and S. C. Parker[1]

1 Department of Chemistry, University of Bath, Claverton Down, Bath BA2 7AY, UK

2 Department of Chemistry, University of Huddersfield, Queensgate, Huddersfield HD1 3DH, UK

3 AWE plc, Aldermaston, Reading, Berkshire RG7 4PR, UK

An important challenge for modelling transport in materials for energy applications is that in most applications they are polycrystalline, and hence it is critical to understand the properties in the presence of grain boundaries. Moreover, most grain boundaries are not pristine stoichiometric interfaces and hence dopants are likely to play a significant role. In this paper, we describe our recent work on using atomistic molecular dynamics simulations to model the effect of doped grain boundaries on oxygen transport of fluorite structured UO2. UO2, much like other fluorite grain boundaries are found to be sinks for oxygen vacancy segregation relative to the grain interior, thus facilitating oxygen transport. Fission products further enhance diffusivity via strong interactions between the impurities and oxygen defects. Doping produces a striking structural alteration in the Σ5 class of grain boundaries that enhances oxygen diffusivity even further. This article is part of the theme issue 'Energy materials for a low carbon future'.

1. Introduction

As of 2018, 66% of the worlds energy is generated from coal, oil and gas, while solar/wind energy is responsible for less than 5% (figure 1) [1]. Rapid expansion of greener alternatives is a necessity in order to reduce the impact of global warming. Nuclear energy plays a vital role in twenty-first century energy production and is responsible for 11.1% of the worlds energy production. Nuclear energy is an established technology that has functioned across the globe for half a century and has the potential to bridge the gap between fossil fuel and renewable technologies for a low carbon future [2]. Despite the ubiquity of nuclear energy production, there are still many poorly understood aspects [3]. Uranium oxide (UO2) is a common polycrystalline energymaterial used in nuclear energy, but it is challenging to work with due to its propensity for oxidation [3]. Ionic transport in polycrystalline materials is a common research question for many energy materials. In UO2 understanding oxygen

transport is key to understanding the corrosion of the fuel. The fluorite lattice of UO2 accommodates additional oxygen with little expansion up to aroundUO2.5 stoichiometry but then undergoes a transition to a layered structure which is associated with a 36% volume increase [4,5]. In a nuclear power plant, this can cause swelling and eventually cracking of fuel rods, which can in turn release harmful contaminants into the environment [6]. Developing a fundamental understanding of oxygen transport properties in UO2 can therefore be used to improve the efficiency, lifespan and, most importantly, safety of nuclear power plants.

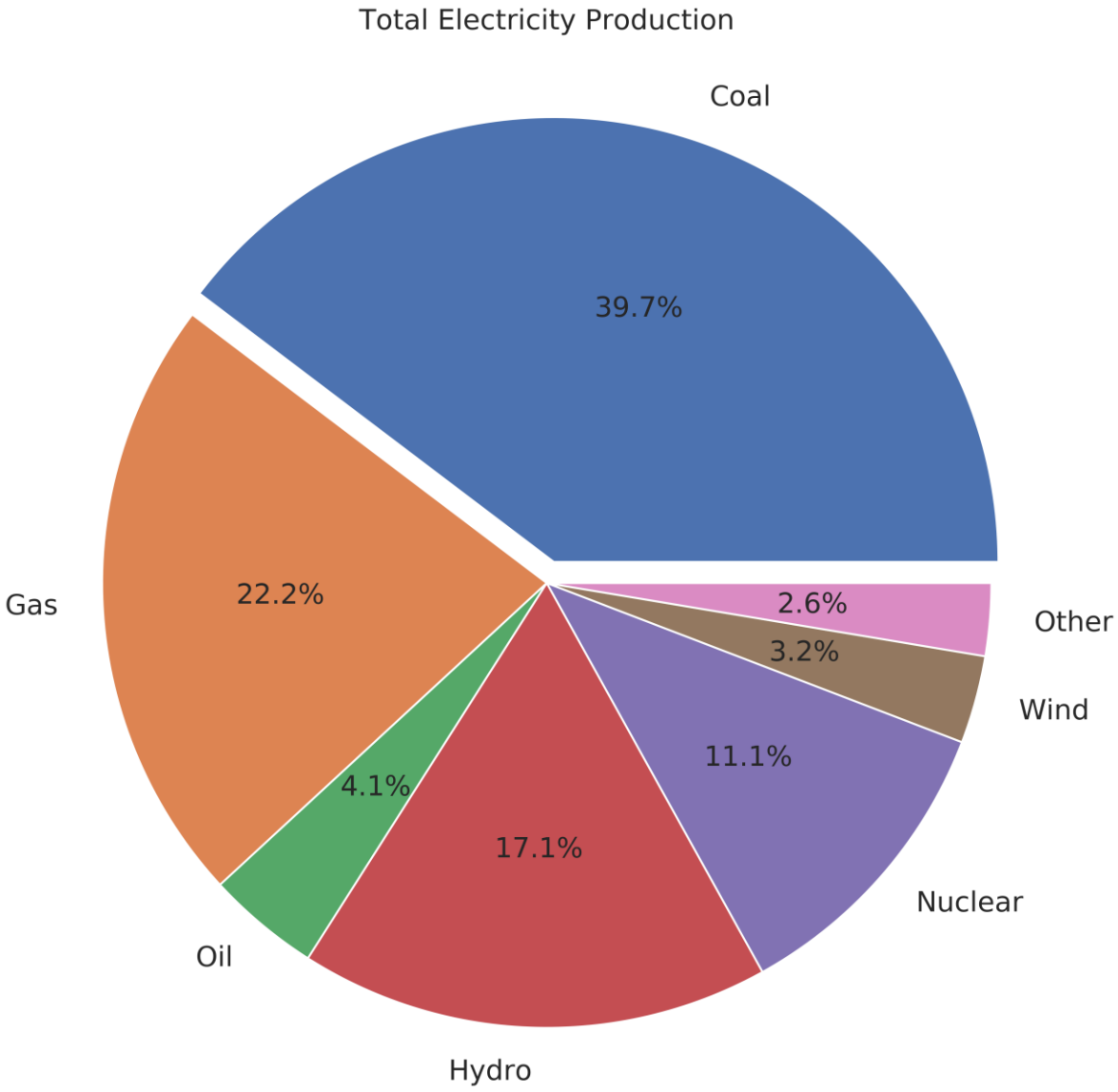

Figure 1. Total contributions to global energy production from coal, gas, oil, hydroelectric, nuclear, wind and other sources. The data were obtained from the global energy database [1].

Although oxygen transport and impurities are well documented in UO2 [7–12], there is no work considering the two phenomena together. The transport properties of GBs have received some attention in recent years but the results have been contradictory. Using experimental techniques, Marin et al., and Sabioni et al. both reported no change in the oxygen transport properties at grain boundaries [7,13]. Whereas, using molecular dynamics studies, Verwerft et al. [14] and Arima et al. [15] both report enhanced oxygen transport at grain boundaries. The latter suggested that this effect was due to the misorientation angle of the grain boundaries.

Further molecular dynamics studies by Vincent-Aublant et al. and Williams el al. have found enhanced diffusion within the grain boundary region at the atomic scale [16,17]. Grain boundaries in other fluorite materials are well studied although there are contrasting interpretations. For example, there are studies stating that it is generally accepted that diffusion along grain boundaries is faster than in the bulk due to the higher defect concentrations and the reduced activation energy of oxygen hops [17,18]. Whereas other studies claim that there is no fast ion diffusion along grain boundaries [19,20]. Furthermore, grain boundaries have been shown to have a blocking effect to ionic transport across the boundary. This is considered to be due to the space charge effect, whereby segregation of charged defects to the grain boundary causes a reduction in ionic transport across the boundary [21–24].

Chemical impurities, i.e. non-stoichiometric cations and anions, are present in high concentrations within UO2, particularly after time within a reactor [25]. Impurities can be introduced to the fuel in three common ways. Fuel fabrication, e.g. fuel pellet sintering. Iron cations are a common impurity, widely reported within UO2 at high concentrations (100–180ppm [26]) and attributed to fuel pellet sintering with steel equipment at high temperatures 1750 $\circ$ C [13,26–36]. A second common way for impurities to enter UO2 is as a fuel poison, e.g. gadolinium, which is a common UO2 dopant, acting as a burnable poison to control the reactivity of fuels in boiling water reactors [37–41]. Gd2O3-doped UO2 has recently been investigated computationally and found to significantly increase the oxygen diffusivity of bulk UO2 [42], furthermore, Th-doped UO2 has also been studied and found to have higher diffusivity [43]. The most common defects are fission products, which are produced during the burning of UO2. There are a wide variety of fission products, and they can be grouped into four categories based upon their chemical state. They can exist as volatile fission products (Kr, Xe, Br, I); metallic precipitates (alloys); ceramic precipitates (oxides based on Rb, Cs, Ba, Zr, Nb, Mo, Te) and oxides dissolved in the fuel (Sr, Zr, Nb, Y, La, Ce, Pr, Nd, Pm, Sm) [44].

There is significant evidence, both experimental and theoretical, which shows that impurities segregate to UO2 grain boundaries [25,45] as well as other fluorite boundaries [46]. Hiernaut

et al. found that fuel oxidation enhanced the segregation of non-soluble fission products from the bulk to the boundaries [47]. Insoluble fission gases such as Xe migrate to grain boundaries where they form bubbles [48,49], Xe can undergo further chain decay leading to other stable fission products, e.g. La/Gd3+ has been shown to segregate to the grain boundaries, resulting in an increase in oxygen conductivity [50]. Recognizing the potential significance of this in this work, we investigate the combination of chemical impurities (fission products and fabrication impurities) within extended structural defects (grain boundaries) and the effect that this combination has on the oxygen transport properties of UO2.

Despite the importance of grain boundaries (GBs) and fission products, their combined effect on the oxygen transport properties of UO2 remains poorly understood and a number of important questions remain. Using large-scale molecular dynamics (MD), we explore the effects of some common impurities (M=M3+, Gd3+ and La3+) on the oxygen diffusivity at grain boundaries in UO2, and we discuss our findings within the broader context of the literature.

2. Methodology

This work employs a classical potential model throughout, derived by Molinari et al. [51] and Williams et al. [17] in the fashion of Pedone et al. [52]. The model is based on rigid ions and uses partial charges (electronic supplementary material, table S1). This model has been shown to accurately reproduce the structural and elastic properties of UO2 [17]. All molecular mechanics calculations, and all models of grain boundaries were generated using the METADISE [53] code as described in detail elsewhere [17,54].

All molecular dynamics simulations (MD) are performed using the DLPOLY code [55]. MD simulations of 5 ns were completed using a timestep of 1 fs with supercells of 8000 species (further information in electronic supplementary material, table S2) and an 8.5Å cut-off. Equilibration was performed using the NPT ensemble until unit cell volume had been converged. Production simulationswere carried out within a temperature range of 2000–3000K at intervals of 250K using the NVT ensemble with a Nose–Hoover thermostat. Cation impurities (Fe3+, Gd3+ and La3+) were substituted onto uranium lattice sites up to a concentration of 1% and were distributed randomly within the grain boundary region (figure 2). This low concentration was chosen to establish whether even a small concentration of dopants will affect oxygen transport, i.e. early stage of corrosion. All details on models are included in electronic supplementary material, table S2. These models are constructed under the approximation that impurities segregate at the boundary as suggested by experimentation [56,57]. Oxygen vacancies were introduced randomly to maintain charge

neutrality throughout the entire structure. Oxygen vacancies reached their equilibrium distribution within the NPT MD simulation, this was confirmed by examining the

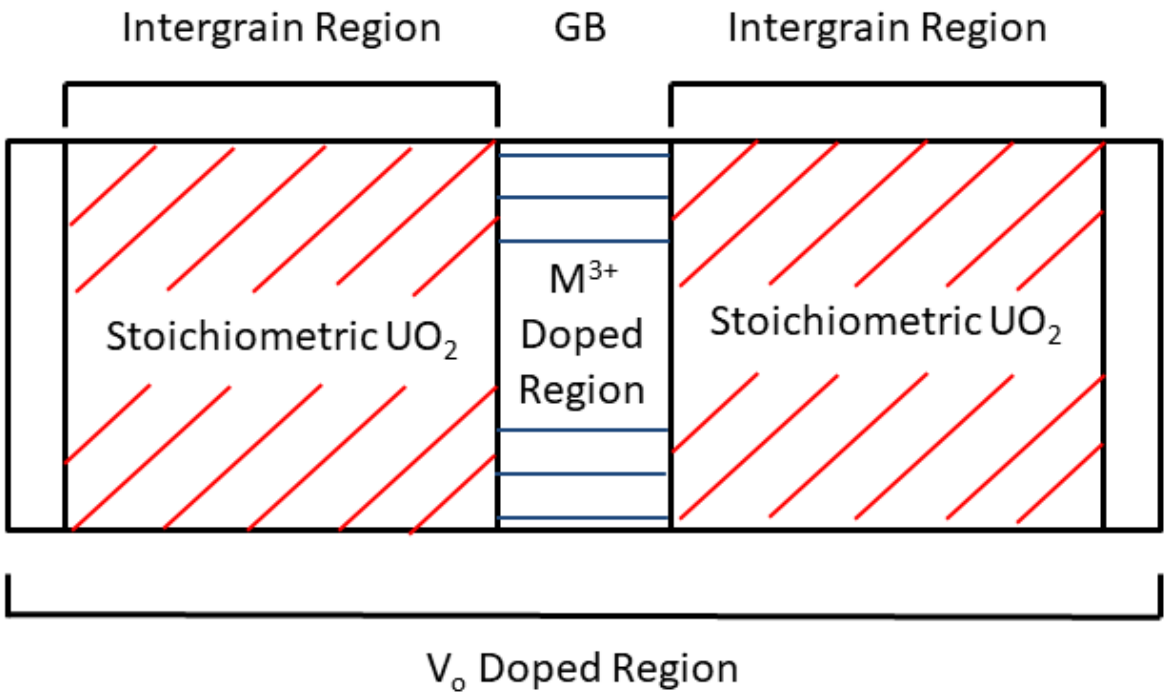

Figure 2. Schematic illustrating the model configuration for grain boundary and doping scheme.

evolution of the oxygen stoichiometry over time. Oxygen vacancies segregated during the early stages of the NPT simulation and this distribution persisted for the duration of the simulation. Tracer-diffusion data for O within grain boundaries was obtained from a regional mean squared displacement (MSD) within the grain boundary according to

$$\langle r_i^2(t)\rangle = 6D_O t, \tag{2.1}$$

where $\langle r_i^2(t)\rangle$ is the MSD, D0 is the diffusion coefficient for oxygen, and t is time. The calculation of the MSD only takes into account those segments of atom trajectories for oxygen species that pass within the grain boundary region.

We use the residence time τ to evaluate the average length of time that an oxygen atom spends in contact with each cation (U4+ and M3+). The τ was calculated from the residence time correlations function, which is defined as

$$\langle R(t)\rangle = \langle \frac{1}{N_0}\sum_{i=1}^{N_t} \theta_i(0)\theta_i(t)\rangle, \tag{2.2}$$

where N is the number of oxygen atoms within a 3Å radius of the cation and Θi(t) is the heavyside function, which is 1 if the ith oxygen atom is in the 3Å radius at t and 0 otherwise. An oxygen atom was only considered to have left the 3Å radius if it did so for at least 2 ps, which allowed molecules that temporarily left then re-entered to be included in τ . Equation (2.2) is integrated to calculate τ .

$$\tau_r = \int_0^{\infty} R(t)dt. \tag{2.3}$$

3. Results

(a) Potential surfaces of grain boundaries

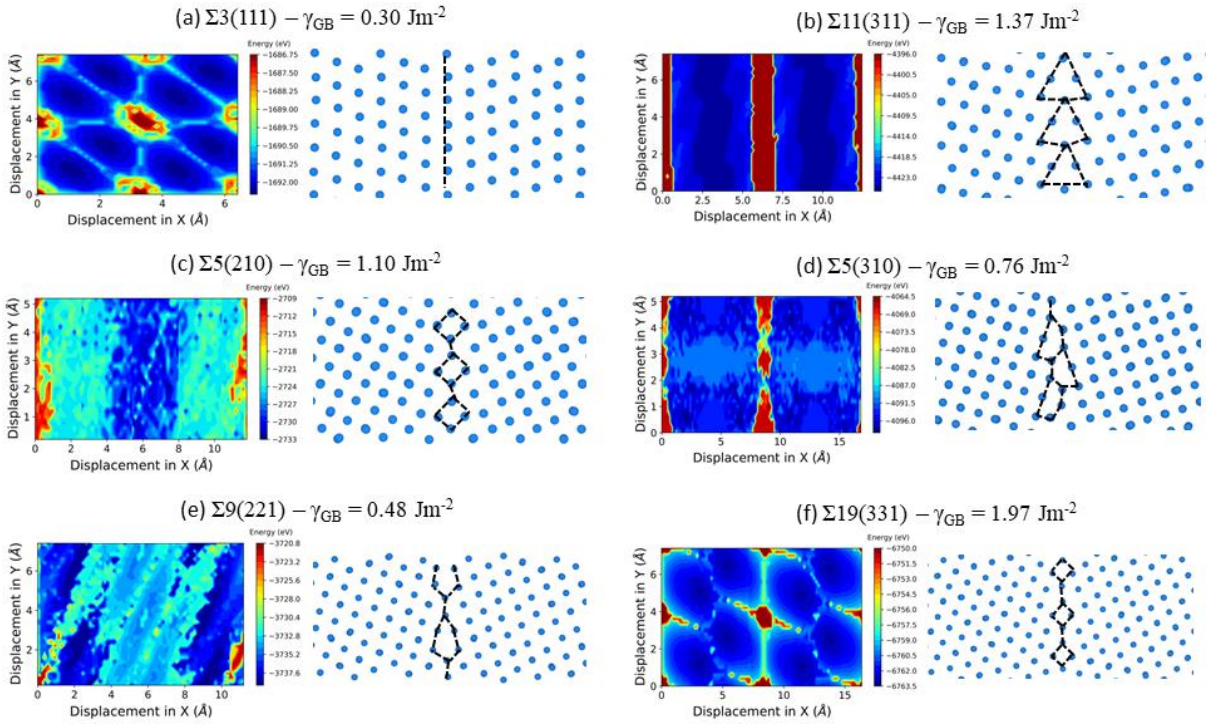

Figure 3. Potential energy surfaces for all grain boundaries (blue and red areas represent low and high energy GB structures)along with their lowest energy structure (only U atoms (blue) shown for clarity) and the grain boundary formation energy.

The Σ3(111), Σ11(311), Σ5(210), Σ5, (310), Σ9(221) and Σ19(331) tilt grain boundary configurations have been constructed according to coincidence site lattice theory [58]. The potential energy surface was probed as a function of displacements of one grain relative to the other in the fashion of Galmarini et al. [54,59]. A two-dimensional grid of energies was constructed to map the complexity of the grain boundary structure. At each point of the grid, a full minimization was carried out and the grain boundary formation energy σGB was calculated using

$$\gamma_{GB} = E_{GB} - E_{Bulk} /2A \quad (3.1)$$

where EGB and EBulk are the energies of the grain boundary configuration and the UO2 bulk simulation cells, respectively, and A is the GB area. A gradient colour map for each boundary is presented in figure 3, where low and high energy grain boundary configurations are highlighted in the blue and red areas; the structures of the lowest energy configurations are also presented for each grain boundary.

The lowest energy grain boundary structures for the Σ3(111), Σ5(210), Σ5(310), Σ9(221) and Σ11(311), show strong resemblance to experimental structures of CeO2, and doped ZrO2 [56,60,61]. The low σGB values of the Σ3 and Σ9 boundaries indicate the presence of high concentrations of these boundaries in UO2 polycrystals in line with experimental SEM analysis of UO2 samples [62].

(b) Grain boundary doped structure

As molecular mechanics calculations do not account explicitly for temperature effects, we have simulated all the lowest energy structures in figure 3 within the molecular dynamics framework. These were first annealed at high temperature and the structures are all consistent with previous calculations [17]. All stoichiometric structures were then doped following the doping scheme illustrated in figure 2. We have also considered a case wherein all impurities are located within the intergrain region of the structure and calculated the energy difference in order to confirm that segregation is energetically feasible. All energies differences are negative, showing that segregation is energetically feasible (figure 4). Doping does not cause any significant structural change with increasing temperature in the Σ3(111), Σ9(221), Σ19(331) and Σ11(311) boundaries. By contrast, the presence of impurities promotes an alteration to the structure of the Σ5(210) grain boundary and a partial structural

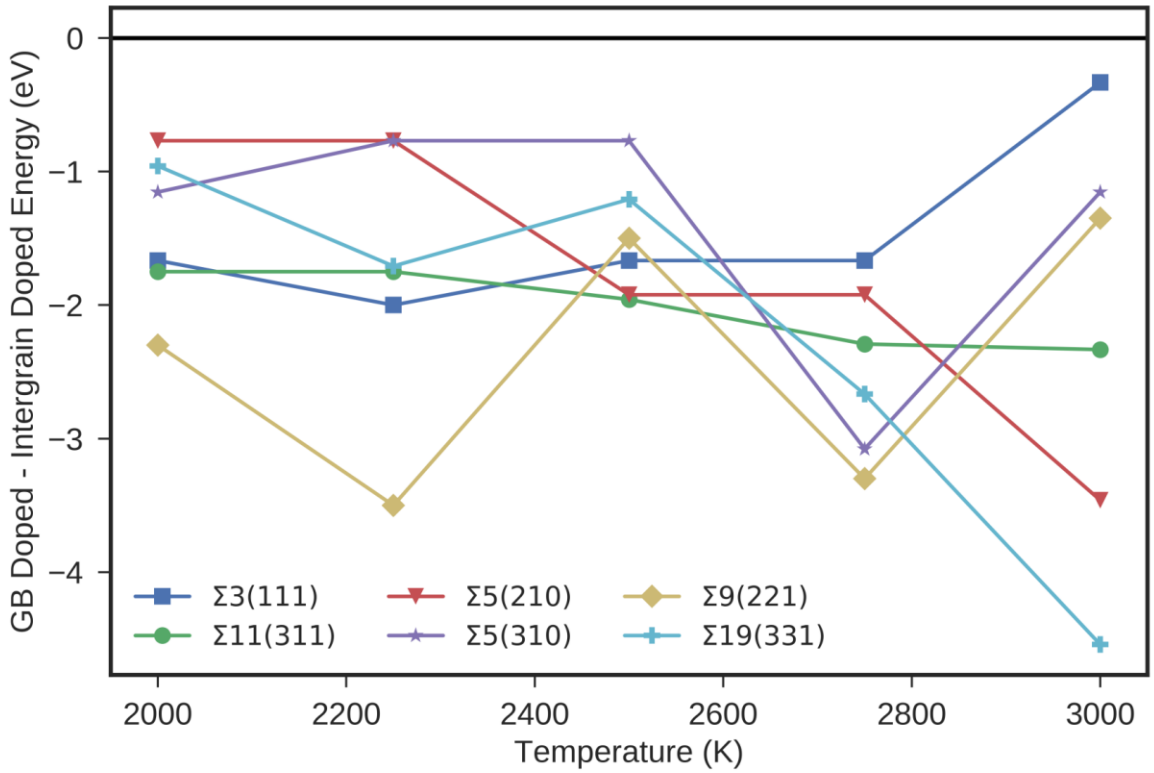

Figure 4. Energy difference between dopants in the doped GB structure and doped IG structure, calculated by subtracting the energy of the intergrain region doped structure from that of the GB-doped structure.

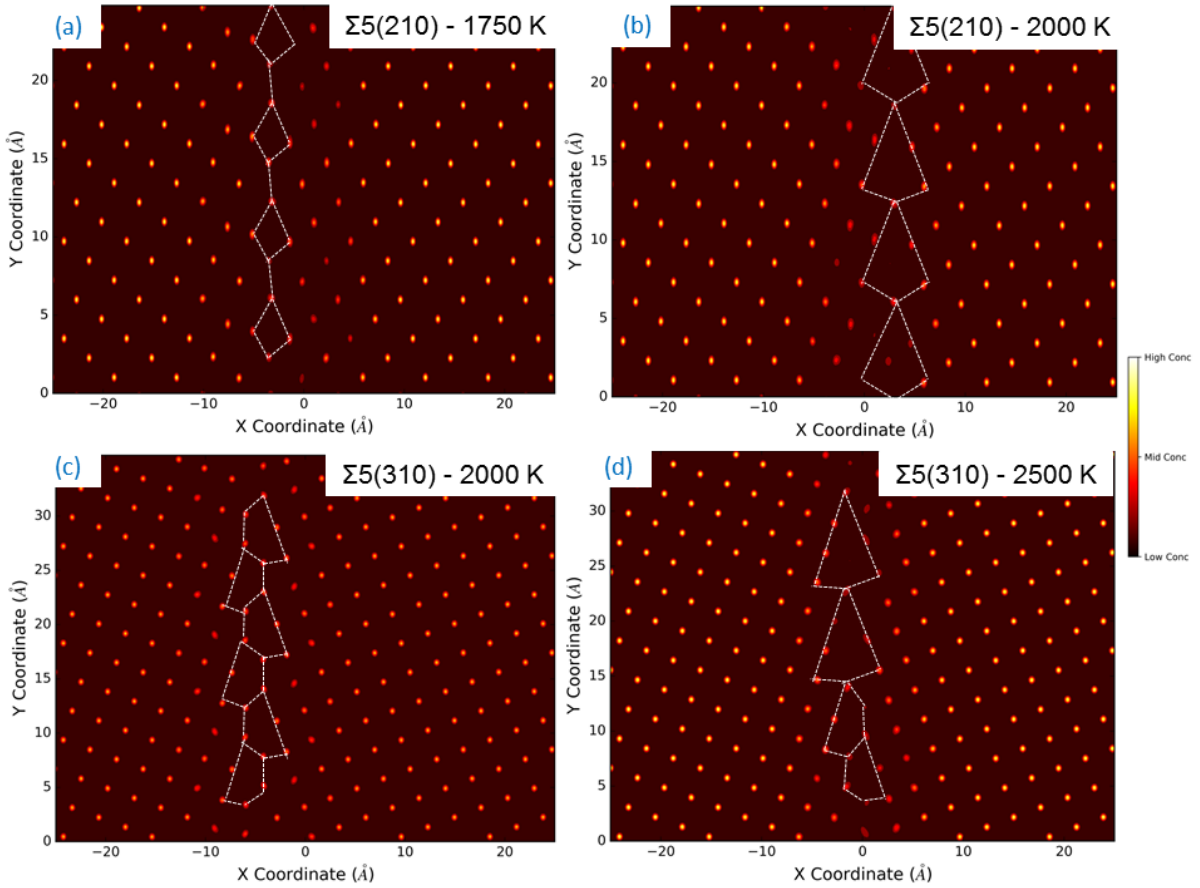

Figure 5. (a,b) Time averaged two-dimensional density profiles of the centre of mass of the cations (U4+/M3+Q1) displayed every 0.5 ps at different temperatures for a 1%Fe3+-dopedΣ5(210) and (c,d)Σ5(310) grain oundaries. The red dots denote the U arrays parallel to the grain boundary plane. Patterns have been drawn to aid visibility.

change in the Σ5(310) grain boundary. figure 5 depicts the time averaged two-dimensional density profiles of the centre of mass of the cations (U4+ /M3+) in the Σ5 grain boundaries at different temperatures. A structural change has been previously reported in the Σ5(210) GB in stoichiometric UO2 and occurs within a temperature range of 2400–2600K [17]; when the structure is doped the transition occurs between 1700 and 2000 K. In the Σ5(310), the partial structural change occurs above 2500K for the doped boundary but it has not been reported in the case of stoichiometric UO2.

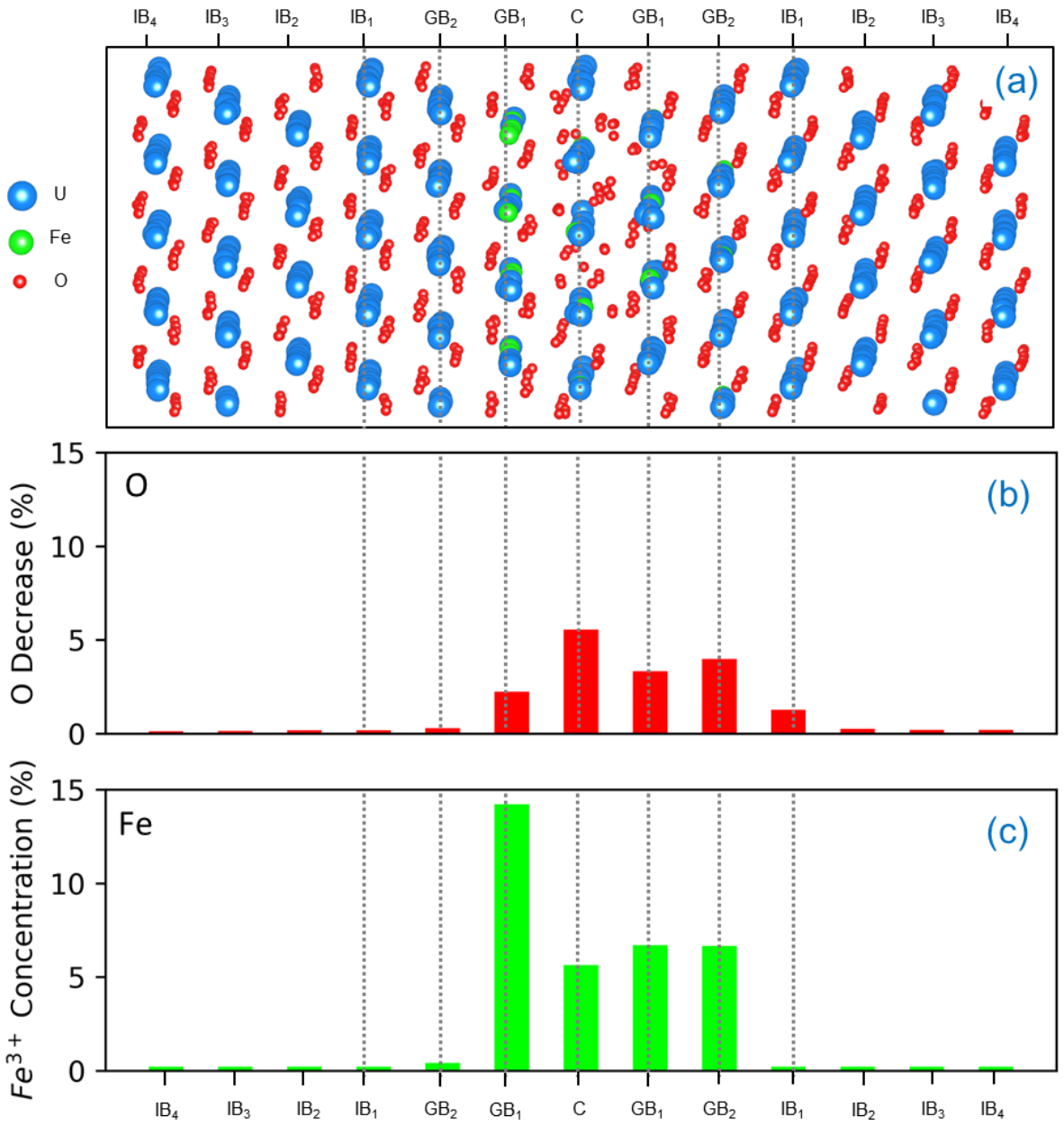

Figure 6. (a) Atomic configuration of Fe-dopedΣ3(111) along [110] direction. (b) Percentage concentration of oxygen vacancies per UO2 layer relative to the stoichiometric structure. (c) Percentage concentration of Fe3+ cation per UO2 layer relative to the stoichiometric structure. For clarity, IB, GB and C refer to UO2 layers in the interboundary region, within the grain boundary width and the grain boundary core, respectively.

The energy map for the two Σ5 boundaries is relatively complicated with many structural configurations within the low energy areas (figure 3). These structural changes as a function of temperature show that impurities stabilize metastable grain boundary configurations, which may not be accessible at low temperature when the structure is stoichiometric.

(c) Oxygen vacancy segregation

Oxygen vacancies were randomly distributed throughout the entire system (figure 2). During the NPT MD simulations which are mobile species, reached their equilibrium position within the doped structure. To quantify the segregation o segregation within the doped grain boundary region, we have evaluated reduction in oxygen concentration for all grain boundaries. As their Q2 behaviour in each boundary is similar, here we present the reduction in oxygen concentration (figure 6b) and Fe distribution (figure 6c) in the grain boundary region compared to the grain interior for the 1% Fe3+-doped Σ3(111) grain boundary (figure 6a). concentration of Fe3+ cation per UO2 layer relative to the stoichiometric structure. For clarity, IB, GB and C refer to UO2 layers in the interboundary region, within the grain boundary width and the grain boundary core, respectively.

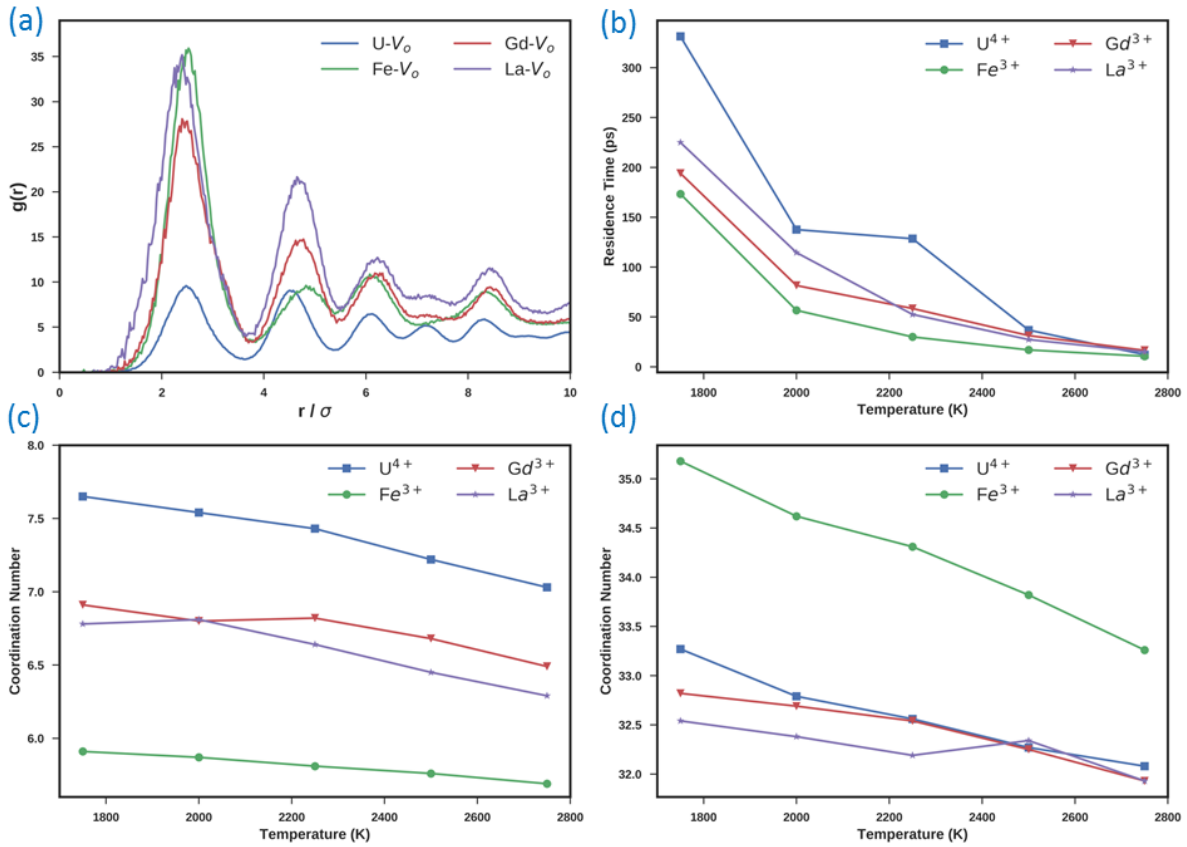

Figure 7. (a) Radial distribution functions for U4+, Fe3+, Gd3+ and La3+ (blue, green, red and purple lines) atoms within the grain boundary region with oxygen vacancies for theΣ3(111) GB. (b–d) Residence time, coordination number in the first (0–3 Å) and second (3–6 Å) shells for oxygen with U4+ (blue squares), Fe3+ (green circles), Gd3+ (red triangles) and La3+ Q1 (purple stars) cations as a function temperature in theΣ3(111) boundary.

The radial distribution functions of cation (figure 7a) were calculated in the fashion of Lucid et al. [63] and provide evidence that theM3+ increases greatly at short distance (i.e. for the nearest neighbours) for all the M3+ compared to the U4+. This is evidence that Vo interact strongly with the impurity compared to the host uranium lattice. Further inspection of the peaks of the radial distribution functions show that in contrast to Fe, La and Gd have also a second intense peak, which is evidence that for these two dopants the interaction with the vacancy is extended to the next-nearest neighbour positions.M3+ defect clusters have been observed experimentally in other M2O3-doped UO2 [64]. This has also been seen for doped CeO2 and linked to the difference in ionic radii of the dopants La3+, Gd3+, Fe3+ (1.061, 0.958, 0.645 Å, respectively) compared to the host cation U4+ (0.89 Å) [65].

We used residence time analysis, i.e. the average time spent by an oxygen atom within the coordination sphere of a cation impurity at the boundaries. We find that oxygen resides longest close to U4+ then La3+ >Gd3+ >Fe3+ (figure 7b) which again follows the atomic radii of the impurity cations. The average coordination number within the first coordination shell (0–3Å from the impurity) and second coordination shell (3–6Å from the impurity) are shown in figure 7c,d. Fe3+ in particular has a significantly lower average CN within the first coordination shell. By contrast, Fe has a higher average CN within the second shell, which supports the RDF data which suggest that oxygen vacancies reside within 3Å of the Fe but up to 6Å for Gd and La. The percentage increase in Vo concentration within the grain boundary region of each structure is presented as a function of temperature (figure 8). There is a common behaviour for our grain boundaries considered, whereby there is an increase in Vo concentration in the grain boundary region. The Σ5(310), Σ9(221), Σ19(331) and Σ11(311) boundaries show a 1.5–2.5% increase in vacancy concentration in the full grain boundary region regardless of the type of impurity up to a temperature of 2750 K, where the oxygen sublattice becomes significantly mobile.

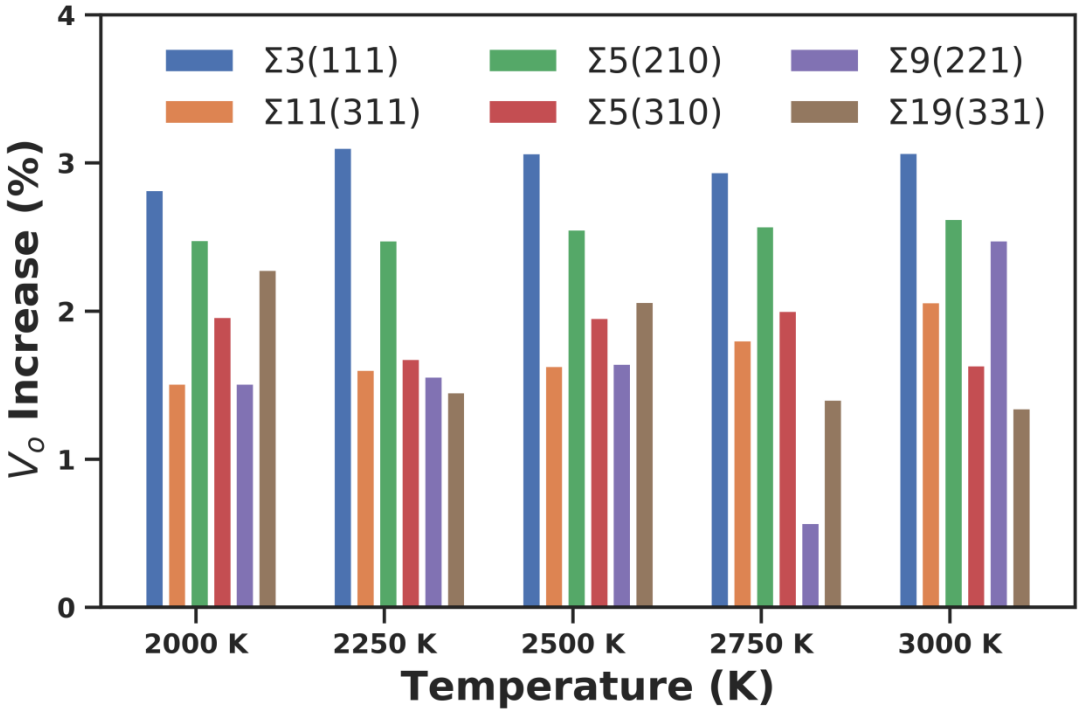

Figure 8. Oxygen vacancy concentration within each grain boundary between 2000 and 3000 K.

To separate the effects of the grain boundary and the impurities, we compared the oxygen stoichiometry of the stoichiometric structures with that of the IG-doped structures mention in figure 4 and found no change in the oxygen concentration at the boundary. This indicates that it is the impurities driving the segregation behaviour in UO2. Vo segregation at grain boundaries is generally accepted for fluorite structures, e.g. Gadolinium-doped ceria (GDC) and Yttria stabilized zirconia (YSZ), in line with the space charge theory [23]. In this work, we have only considered the segregation behaviour of oxygen vacancies at grain boundaries and we have not calculated the electrostatic potential and the space charge effect. Arora & Aidhy [66] studied the energetics of Vo within UO2 grain boundaries and found vacancy segregation favourable when compared to the bulk material. Several other studies have reported within doped grain boundary systems [67–71]. This represents the first time that impurity promoted oxygen vacancy segregation at the grain boundaries has been proposed in UO2.

(d) Oxygen diffusion at grain boundaries

Our modelling results show that impurities significantly increase the oxygen transport within the grain boundaries. A simple visual representation is shown in figure 9 where a single GB oxygen atom over a 1 ns trajectory is depicted in grey for a stoichiometric (figure 9a) and 1% Fe3+-doped (figure 9b) grain boundary. This shows that there is localization of the

oxygen diffusing species only in the grain boundary region, thus the grain boundaries act as a sink for vacancies. This behaviour is consistent with other studies investigating the effect of space charge on transport [24].

The oxygen diffusion coefficients are shown in electronic supplementary material, figure S1 for all the grain boundary configurations. We find that the diffusion enhancement in stoichiometric boundaries follows the order Σ3(111)>Σ9(221)>Σ19(331)>Σ11(311)>Σ5(310)>Σ5(210) at a representative temperature of 2500 K. There is a significant difference in the diffusion coefficient of the grain boundaries, with a 1 order of magnitude difference between the lowest value of 0.049 × 10−9 ms−2 obtained for the Σ5(210) and the highest value of 0.53 × 10−9 ms−2 found for the Σ3(111) at 2500 K. Impurity cations further increase the diffusion within the grain boundary with Fe3+ having a greater effect than La3+ and Gd3+. The increase corresponds to 0.1 × 10−9 ms−2 for the Σ3(111), Σ9(221), Σ19(331), Σ11(311) boundaries and 0.5 × 10−9 ms−2 for the Σ5(210) and Σ5(310) boundaries. The large increase in the Σ5 series is due to the Σ5 structural changes discussed in §3a (figure 10).

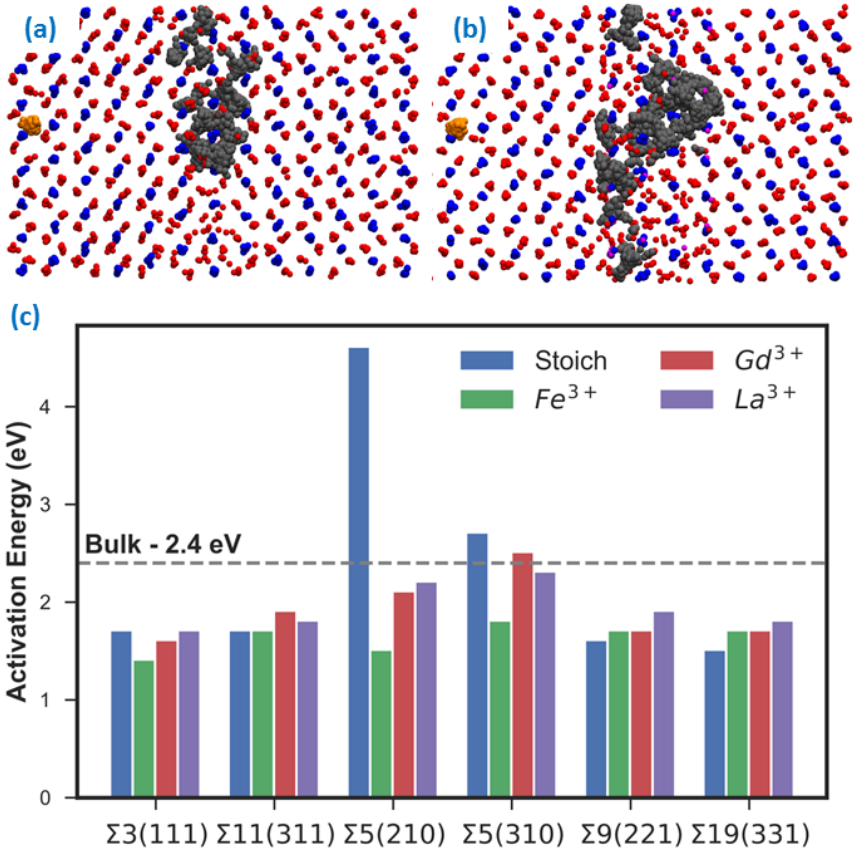

Figure 9. (a,b) Structure of the stoichiometric and 1% Fe3+-doped Σ3(111) grain boundary structures. For clarity, oxygen, uranium and iron atoms are shown in red, blue and pink, respectively. To illustrate the effect of the grain boundary on diffusion, the full trajectory

across 1 ns for a single oxygen atom has been shown for a grain boundary oxygen (grey) and an interboundary oxygen (orange). (c) Activation energies for the stoichiometric (blue), Fe3+ (green), Gd3+ (red) and La3+ (purple) doped grain boundary regions compared to the activation energy of oxygen Q1 diffusion in 1% M3+-doped bulk O2 (2.4 eV).

The calculated activation energy for a 1% concentration of M3+-doped bulk UO2 is 2.4 eV. While this is the activation energy of a UO2−x system and a comparison should be treated with caution, the activation energy of stoichiometric UO2 calculated experimentally −2.60 eV should be noted [72]. For clarity, we only present activation energies for oxygen diffusion within the grain boundary region (figure 9c). There is a general decrease in activation energy (Ea) from the stoichiometric bulk (2.4 eV) to the grain boundaries with the exception of the Σ5(210) and Σ5(310) boundaries. The stoichiometric Σ3(111)/Σ11(311) and Σ9(221)/Σ19(331) boundaries have similar Ea −1.7 and 1.6 eV, which is approximately half that of the intergrain region. Fe3+ and Gd3+ cause a small decrease in Ea in the Σ3(111) boundary, while La3+ has no effect. With the exception of Fe3+ in the Σ11(311) boundary, impurities cause a small increase in Ea in the Σ9(221), Σ19(331) and Σ11(311) grain boundaries compared to their stoichiometric counterparts. So while the impurities are promoting increased diffusivity, the activation energy is for the most part unchanged or slightly increased. For the stoichiometric Σ5 boundaries, there is a particularly high Ea, 4.3 and 2.7 eV for the Σ5(210) and Σ5(310), respectively, highlighting the poor transport properties of these boundaries.

This shows that the Σ5 boundaries are blocking oxygen transport. Upon the introduction of impurities, there is a large decrease in the Ea for both the Σ5(210) boundary and a modest decrease for the Σ5(310) boundary, which we infer is due to the structural change discussed in §3a. In our previous work, we reported modest increases in transport in small segments of the Σ5 boundaries at short timescales. This work highlights that at long timescales when considering the boundary as a single structure, there is a blocking effect.

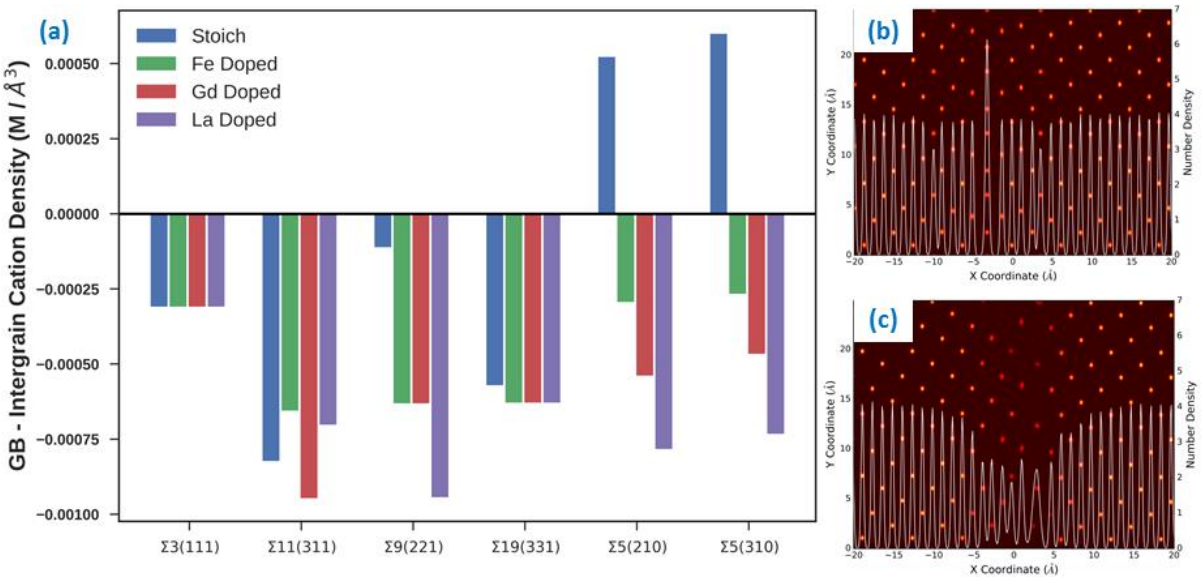

Figure 10. Cation density difference between the intergrain region and the grain boundary region a). Time averaged two dimensional density profiles of the centre of mass of both U and M3+ displayed every 0.5 ps at different temperatures, overplayed with the one-dimensional uranium density profile for the stoichiometric (b) and 1% Fe doped (c)Σ5(210).

A possible explanation for the low diffusivity in the Σ5 boundaries relates to the cation density at the boundary compared with the inter-boundary region. Upon going from the interboundary region to the grain boundary in the Σ3, Σ9, Σ11 and Σ19 boundaries, there is a slight decrease in cation density. Whereas in the Σ5 boundaries, there is an increase in cation density (figure 10). Upon introduction of impurities, there is a decrease in the cation density at the boundary due to a small increase in grain boundary width (figure 10c). Relating the cation density at the grain boundary to the transport properties of boundaries provides a possible explanation for the blocking nature of the Σ5.

4. Discussion

We studied the early stage of segregation of impurities at grain boundaries, and we demonstrated that even at a concentration as low as 1%, there is segregation of oxygen vacancies and an increase of local oxygen diffusion that will impact the oxygen storage capacity of the fuel and so the availability of oxygen to enter the corrosion process. Our results demonstrate that the impurity content of UO2 can have important implications for the corrosion of nuclear material. Our work illustrates the importance of the pre reactor stage of the fuel cycle. Fe3+ is a potentially avoidable impurity that is found in all fuels as a result of the fuel pellet sintering. It has been shown that the amount of Fe within the fuel pellets can be reduced by different fabrication processes, e.g. high levels of Fe are characteristic of fuel produced by dry chemical conversion compared to other methods such as the water or gas flame methods [26]. Fabrication plants typically have a purity limit

(generally 1250ppm [73]). Given that impurities segregate to the grain boundaries [24,45], there will be high local concentrations of impurity within the grain boundaries, opposed to an homogeneous distribution of the impurity in the grain interiors. Based upon these results, sintering methods that minimize the inclusion of Fe within the UO2 pellet are crucial to increasing the safety and lifetime of the fuel. Unlike Fe3+, our results add further evidence to previous experimental and theoretical studies that Gd3+ is enhancing the oxygen transport within the fuel and thus the corrosion. We have also provided information on the state of the grain boundaries within irradiated UO2. The presence of La3+ in UO2 is unavoidable as it forms through fission chain decay within the reactor [74]. These results show that La3+ will increase the corrosion through oxygen diffusion and in the case of the Σ5 boundaries cause structural changes. Experimental studies of post reactor fuel should pay careful attention to La3+ concentration within the spent fuel as its presence could indicate unstable grain boundary systems.

These results can be expected to be applicable to the wider field of fluorite grain boundaries. While it is accepted that transport along grain boundaries is higher than bulk transport, transport across the grain boundaries is blocked by the space charge effect. The space charge effect is well documented in CeO2−x and doped zirconia and is due to the segregation of charged defects to the grain boundary [22–24]. This causes a blocking effect of transport across the boundary. Our results show that theM3+ cations present at the boundary strongly attract oxygen vacancies (figures 6–8), pulling them to the boundary where they will remain trapped and facilitate high levels of oxygen transport along the boundary and thereby increase the rate of corrosion. Kubo et al. has seen a similar effect in UO2 whereby at Gd3+ concentrations at or exceeding 10 wt%, a potential barrier for the migration of electron holes formed [50]. This suggests that this behaviour (i.e. segregation o at grain boundaries and high diffusion in the grain boundary region) is indeed common to the fluorite structure and thus cation independent, whether U, Ce, Zr. Space charge can be probed Q3 using molecular dynamics simulations by calculating the electrostatic potential from the atomic trajectories. This therefore presents an avenue for future study on this topic.

5. Conclusion

The atomistic effects of grain boundaries are important to fully understand the transport properties of UO2. Enhancing our fundamental understanding of these interfaces and their influence on oxygen ion transport is crucial for the future optimization of new nuclear fuel materials. In this study, we have quantified this effect using large-scale MD simulations. Our results support three key features. A common feature of a grain boundary structure is the segregation of oxygen vacancies at grain boundary regions, promoted by the impurity cations.

Which is related to the energetic preference for impurities to have a lower oxygen coordination number. The presence of different sites at the grain boundary provides a way for the material to accommodate the strain induced by the impurities. This increase in charge carriers (oxygen vacancies) induces an enhanced oxygen diffusivity which is localized at the grain boundary regions. Finally, there are structural changes occurring as a function of temperature for $\Sigma 5$ grain boundaries, which are facilitated by the presence of impurities; as the potential energy surface of these boundaries is complex, the presence impurity lowers the grain boundary energy allowing more structural configurations to be explored during the molecular dynamics simulation.

Our modelling shows that GB are areas of fast ionic diffusion and thusmay enhance corrosion. As the material starts corroding, oxygen enters via the grain boundaries and diffuses out into the individual grains and ultimately form higher oxide phases, which has been predicted previously [75]. Impurities within grain boundaries will, based upon our results increase this process and ultimately accelerate the degradation of the fuel.

Data accessibility. Force field parameters, atomic configurations, diffusion coefficients and Arrhenius plots can be found in the electronic supplementary material. Atomic density analysis and the mean squared displacements were carried out using the polypy code [76].

Authors' contributions. A.R.S. carried out the simulations, performed the data analysis and wrote the manuscript with contributions from all authors; S.C.P., M.M. and A.R.S. designed the study; M.M. and S.C.P. derived the force fields used in the study.

Competing interests. The authors declare that they have no competing interests.

Funding. A.R.S. acknowledges AWE and EPSRC (EP/R010366/1) for funding. Computations were run on Balena HPC facility at the University of Bath and the ARCHER UK National Supercomputing Service (http://www.archer.ac.uk) via our membership of the UK's HEC Materials Chemistry Consortium funded by EPSRC (EP/L000202).

Acknowledgements. M.M. thanks the University of Huddersfield for access to computing facility.

References

1. Aaron K. 2018 Global power plant database. Global Energy Observatory, Google, KTH Royal

Institute of Technology in Stockholm, Enipedia, World Resources Institute. (http://datasets.wri.

org/dataset/globalpowerplantdatabase)

2. Gralla F, Abson DJ, Møller AP, Lang DJ, vonWehrdenH. 2017 Energy transitions and national

development indicators: a global review of nuclear energy production. Renew. Sust. Energy

Rev. 70, 1251–1265. (doi:10.1016/j.rser.2016.12.026)

3. Guerin Y,Was GS, Zinkle SJ. 2009 Materials challenges for advanced nuclear energy systems.

MRS Bull. 34, 10–19.

4. Brincat NA, Molinari M, Allen GC, Molinari MT, Parker SC. 2015 Density functional

theory calculations of defective UO2 at U3O7 stoichiometry. J. Nucl. Mater. 467, 724–729.

(doi:10.1016/j.jnucmat.2015.10.006)

5. Brincat NA, Parker SC, Molinari M, Allen GC, Storr MT. 2015 Density functional theory

investigation of the layered uranium oxides U3O8 and U2O5. Dalton Trans. 44, 2613–2622.

(doi:10.1039/C4DT02493A)

6. Taylor P, Wood DD, Duclos AM, Owen DG. 1989 Formation of uranium trioxide

hydrates on UO2 fuel in airsteam mixtures near 200 ◦ C. J. Nucl. Mater. 168, 70–75.

(doi:10.1016/0022-3115(89)90566-7)

7. Marin JF, Contamin P. 1969 Uranium and oxygen self-diffusion in UO2. J. Nucl. Mater. 30,

16–25. (doi:10.1016/0022-3115(69)90164-0)

8. Bertolus M et al. 2015 Linking atomic and mesoscopic scales for the modelling of the

transport properties of uranium dioxide under irradiation. J. Nucl. Mater. 462, 475–495.

(doi:10.1016/j.jnucmat.2015.02.026)

9. Perriot R, Liu XY, Stanek CR, Andersson DA. 2015 Diffusion of Zr, Ru, Ce, Y, La, Sr and Ba

fission products in UO2. J. Nucl. Mater. 459, 90–96. (doi:10.1016/j.jnucmat.2015.01.001)

10. Rest J, Cooper MWD, Spino J, Turnbull JA, Van Uffelen P, Walker CT. 2018 Fission

gas release from UO2 nuclear fuel: a review. J. Nucl. Mater. 513, 310–345. (doi:10.1016/

j.jnucmat.2018.08.019)

11. Catlow CRA, JS Anderson. 1977 Point defect and electronic properties of uranium dioxide.

Proc. R. Soc. Lond. A 353, 533–561. (doi:10.1098/rspa.1977.0049)

12. Catlow CRA, WC Marshall. 1978 Fission gas diffusion in uranium dioxide. Proc. R. Soc. Lond.

A 364, 473–497. (doi:10.1098/rspa.1978.0213)

13. Sabioni ACS, Ferraz WB, Millot F. 2000 Effect of grain boundaries on uranium and

oxygen diffusion in polycrystalline UO2. J. Nucl. Mater. 278, 364–369. (doi:10.1016/S0022-

3115(99)00250-0)

14. Govers K, Verwerft M. 2013 Classical molecular dynamics investigation of microstructure

evolution and grain boundary diffusion in nano-polycrystalline UO2. J. Nucl. Mater. 438,

134–143. (doi:10.1016/j.jnucmat.2013.03.024)

15. Arima T, Yoshida K, Idemitsu K, Inagaki Y, Sato I. 2010 Molecular dynamics analysis of

diffusion of uranium and oxygen ions in uranium dioxide. In IOP Conference Series: Materials

Science and Engineering, vol. 9, p. 012003. Q4

16. Vincent-Aublant E, Delaye JM, Van Brutzel L. 2009 Self-diffusion near symmetrical tilt grain

boundaries in UO2 matrix: a molecular dynamics simulation study. J. Nucl. Mater. 392,

114–120. (doi:10.1016/j.jnucmat.2009.03.059)

17. Williams NR, Molinari M, Parker SC, Storr MT. 2015 Atomistic investigation of the structure

and transport properties of tilt grain boundaries of UO2. J. Nucl. Mater. 458, 45–55.

(doi:10.1016/j.jnucmat.2014.11.120)

18. Duffy DM. 1986 Grain boundaries in ionic crystals. J. Phys. Condens. Matter 19, 4393–4412.

(doi:10.1088/0022-3719/19/23/005)

19. De Souza RA, Pietrowski MJ, Anselmi-Tamburini U, Kim S, Munir ZA, Martin M. 2008

Oxygen diffusion in nanocrystalline yttria-stabilized zirconia: the effect of grain boundaries.

Phys. Chem. Chem. Phys 10, 2067–2072. (doi:10.1039/b719363g)

20. Dura OJ, Lopez de la TorreMA, Vazquez L, Chaboy J, Boada R, Rivera-Calzada A, Santamaria

J, Leon C. 2010 Ionic conductivity of nanocrystalline yttria-stabilized zirconia: grain boundary

and size effects. Phys. Rev. B 81, 184301. (doi:10.1103/PhysRevB.81.184301)

21. Lin Y, Fang S, Su D, Brinkman KS, Chen F. 2015 Enhancing grain boundary ionic conductivity

in mixed ionic–electronic conductors. Nat. Commun. 6, 6824. (doi:10.1038/ncomms7824)

22. Guo X, Sigle W, Maier J. 2003 Blocking grain boundaries in yttria-doped and undoped ceria

ceramics of high purity. J. Am. Ceram. Soc. 86, 77–87. (doi:10.1111/jace.2003.86.issue-1)

23. Guo X, Sigle W, Fleig J, Maier J. 2002 Role of space charge in the grain boundary blocking effect

in doped zirconia. J. Solid State Ion. 154–155, 555–561. (doi:10.1016/S0167-2738(02)00491-5)

24. De-Souza RA. 2009 The formation of equilibrium space-charge zones at grain boundaries in

the perovskite oxide SrTiO3. Phys. Chem. Chem. Phys. 11, 9939–9969. (doi:10.1039/b904100a)

25. Ewing RC. 2015 Longterm storage of spent nuclear fuel. Nat. Mater. 14, 252–257.

(doi:10.1038/nmat4226)

26. Pajo L. 2018 UO2 Fuel pellet impurities, pellet surface roughness and n(18O)/n(16O) ratios,

applied to nuclear forensic science.

27. Auskern AB, Belle J. 1961 Uranium ion self diffusion in UO2. J. Nucl. Mater. 3, 311–319.

(doi:10.1016/0022-3115(61)90199-4)

28. Ray ILF, Thiele H,Matzke H. 1992 Transmission electron microscopy study of fission product

behaviour in high burnupUO2. J. Nucl.Mater. 188, 90–95. (doi:10.1016/0022-3115(92)90458-W)

29. Evans AG, Davidge RW. 1969 The strength and fracture of stoichiometric polycrystalline UO2.

J. Nucl. Mater. 33, 249–260. (doi:10.1016/0022-3115(69)90019-1)

30. Wronkiewicz DJ, Bates JK, Gerding TJ, Veleckis E, Tani BS. 1992 Uranium release and

secondary phase formation during unsaturated testing of UO2 at 90 ◦ C. J. Nucl. Mater. 190,

107–127. (doi:10.1016/0022-3115(92)90081-U)

31. Ainscough JB, Oldfield BW, Ware JO. 1973 Isothermal grain growth kinetics in sintered UO2

pellets. J. Nucl. Mater. 49, 117–128. (doi:10.1016/0022-3115(73)90001-9)

32. Wronkiewicz DJ, Bates JK,Wolf SF, Buck EC. 1996 Ten year results from unsaturated drip tests

with UO2 at 90C: implications for the corrosion of spent nuclear fuel. J. Nucl.Mater. 238, 78–95.

(doi:10.1016/S0022-3115(96)00383-2)

33. Radford KC, Pope JM. 1983 UO2 fuel pellet microstructure modification through impurity

additions. J. Nucl. Mater. 116, 305–313. (doi:10.1016/0022-3115(83)90116-2)

34. Hastings IJ, Scoberg JA, MacKenzie K. 1979 Grain growth in UO2: in reactor and laboratory

testing. J. Nucl. Mater. 82, 435–438. (doi:10.1016/0022-3115(79)90026-6)

35. Cannon RF, Roberts JTA, Beals RJ. 1971 Deformation of UO2 at high temperatures. J. Am.

Ceram. Soc. 54, 105–112. (doi:10.1111/jace.1971.54.issue-2)

36. Nogita K, Une K. 1993 Thermal recovery of radiation defects and microstructural change in

irradiated UO2 fuels. Nucl. Sci. Tech. 30, 900–910. (doi:10.1080/18811248.1993.9734564)

37. Kloosterman JL. 2003 Application of boron and gadolinium burnable poison particles

in UO2 and PUO2 fuels in HTRs. Ann. Nucl. Energy 30, 1807–1819. (doi:10.1016/S0306-

4549(03)00134-8)

38. Durazzo M, Riella HG. 2001 Effect of mixed powder homogeneity on the UO2 Gd2O3

nuclear fuel sintering behavior. Key Eng. Mater. 189–191, 60–66. (doi:10.4028/www.scientific.

net/KEM.189-191)

39. Asou M, Porta J. 1997 Prospects for poisoning reactor cores of the future. J. Nucl. Eng. Des. 168,

261–270. (doi:10.1016/S0029-5493(96)01322-2)

40. Wakabayashi T, Minatsuki I. 1983 Critical experiments on gadolinium poisoned cluster type

fuel assemblies in heavy water lattices. Nucl. Sci. Tech. 83, 50–62.

41. Riella HG, Durazzo M, Hirata M, Nogueira RA. 1991 Effect of mixed powder homogeneity

on the UO2 Gd2O3 nuclear fuel sintering behavior. J. Nucl. Mater. 178, 204–211.

(doi:10.1016/0022-3115(91)90387-M)

42. Galvin COT, Cooper MWD, Rushton MJD, Grimes RW. 2018 Oxygen diffusion in Gd-doped

mixed oxides. J. Nucl. Mater. 498, 300–306. (doi:10.1016/j.jnucmat.2017.10.036)

43. Cooper MWD, Murphy ST, Fossati PCM, Rushton MJD, Grimes RW. 2014 Thermophysical

and anion diffusion properties of UxTh1-xO2. Proc. R. Soc. A 470, 20140427.

(doi:10.1098/rspa.2014.0427)

44. Kleykamp H. 1985 The chemical state of the fission products in oxide fuels. J. Nucl.Mater. 131,

221–246. (doi:10.1016/0022-3115(85)90460-X)

45. Hong M, Uberuaga BP, Phillpot SR, Andersson DA, Stanek CR, Sinnott SB. 2013 The role

of charge and ionic radius on fission product segregation to a model UO2 grain boundary.

J. Appl. Phys. 113, 134902. (doi:10.1063/1.4798347)

46. Avila-Paredes HJ, Kim S. 2006 The effect of segregated transition metal ions on the grain

boundary resistivity of gadolinium doped ceria: Alteration of the space charge potential. Solid

State Ion. 177, 3075–3080. (doi:10.1016/j.ssi.2006.08.017)

47. Hiernaut JP, Wiss T, Papaioannou D, Konings RJM, Rondinella VV. 2008 Volatile fission

product behaviour during thermal annealing of irradiated UO2 fuel oxidised up to U3O8.

J. Nucl. Mater. 372, 215–225. (doi:10.1016/j.jnucmat.2007.03.174)

48. Lidiard AB. 1966 Self diffusion of uranium in UO2. J. Nucl. Mater. 19, 106–108.

(doi:10.1016/0022-3115(66)90138-3)

49. Nerikar PV, Parfitt DC, Casillas Trujillo LA, Andersson DA, Unal C, Sinnott SB, Grimes RW,

Uberuaga BP, Stanek CR. 2011 Segregation of xenon to dislocations and grain boundaries in

uranium dioxide. Phys. Rev. B 84, 174105. (doi:10.1103/PhysRevB.84.174105)

50. Kubo T, Ishimoto S, Ama TKOY. 1993 Effects of gadolinium doping on electrical properties of

UO2 grain boundaries. Nucl. Sci. Tech. 30, 664–672. (doi:10.1080/18811248.1993.9734532)

51. Sayle TXT, Molinari M, Das S, Bhatta UM, Möbus G, Parker SC, Seal S, Sayle DC. 2013

Environment mediated structure, surface redox activity and reactivity of ceria nanoparticles. Nanoscale 5, 6063. (doi:10.1039/c3nr00917c)

52. Pedone A, Malavasi G, Menziani MC, Cormack AN, Segre U. 2006 A new self-consistent empirical interatomic potential model for oxides, silicates, and silica-based glasses. J. Phys. Chem. B 110, 11780. (doi:10.1021/jp0611018)

53. Watson GW, Kelsey ET, deLeeuw NH, Harris DJ, Parker SC. 1996 Atomistic simulation of dislocations, surfaces and interfaces in MgO. J. Chem. Soc. Faraday Trans. 92, 433–438. (doi:10.1039/ft9969200433)

54. Galmarini S, Aschauer U, Bowen P, Parker SC. 2008 Atomistic simulation of Y-doped a-alumina interfaces. J. Am. Ceram. Soc. 91, 3643–3651. (doi:10.1111/jace.2008.91.issue-11)

55. Smith W, Forester TR. 1996 DL POLY 2.0: a general purpose parallel molecular dynamics

simulation package. J. Mol. Graph. 14, 136–141. (doi:10.1016/S0263-7855(96)00043-4)

56. Feng B, Yokoi T, Kumamoto A, Yoshiya M, Ikuhara Y, Shibata N. 2016 Atomically ordered solute segregation behaviour in an oxide grain boundary. Nat. Commun. 7, 11079. (doi:10.1038/ncomms11079)

57. Shibata N, Ikuhara Y, Oba F, Yamamoto T, Sakuma T. 2002 Atomic structure and solute

segregation of a Σ =3, [110]/111 grain boundary in an yttria-stabilized cubic zirconia

bicrystal. Philos. Mag. 82, 393–414. (doi:10.1080/01418610208239607)

58. Brokman A, Balluffi RW. 1981 Coincidence lattice model for the structure and energy of grain

boundaries. Acta Mater. 29, 1703–1719. (doi:10.1016/0001-6160(81)90005-5)

59. Yeandel SR, Molinari M, Parker SC. 2018 The impact of tilt grain boundaries on the thermal

transport in perovskite SrTiO3 layered nanostructures. A computational study. Nanoscale 10,

15 010–15 022. (doi:10.1039/C8NR02234H)

60. Shibata N, Oba F, Yamamoto T, Ikuhara Y. 2004 Structure, energy and solute segregation

behaviour of [110] symmetric tilt grain boundaries in yttria-stabilized cubic zirconia. Philos.

Mag. 84, 2381–2415. (doi:10.1080/14786430410001693463)

61. Fisher CAJ, Matsubara H. 1999 The influence of grain boundary misorientation on ionic

conductivity in YSZ. J. Eur. Ceram. Soc. 19, 703–707. (doi:10.1016/S0955-2219(98)00300-8)

62. Nerikar PV et al. 2011 Grain boundaries in uranium dioxide: scanning electron

microscopy experiments and atomistic simulations. J. Am. Ceram. Soc. 94, 1893–1900.

(doi:10.1111/jace.2011.94.issue-6)

63. Lucid AK, Watson GW. 2017 The importance of polarizability in the modeling of ionic

diffusion in ceria. In IOP Conference Series: Materials Science and Engineering, vol. 169, p. 012002. Q4

64. Razdan M, Shoesmith DW. 2014 Influence of trivalent dopants on the structural and

electrochemical properties of uranium dioxide (UO2). J. Electrochem. Soc. 161, 105–113.

(doi:10.1149/2.047403jes)

65. Minervini L, Zacate MO, Grimes RW. 1999 Defect cluster formation in M2O3-doped CeO2.

Solid State Ion. 116, 339–349. (doi:10.1016/S0167-2738(98)00359-2)

66. Arora G, Aidhy SD. 2017 Segregation and binding energetics at grain boundaries in fluorite

oxides. J. Mater. Chem. A 5, 4026–4035. (doi:10.1039/C6TA09895A)

67. Yoshiya M, Oyama T. 2011 Impurity and vacancy segregation at symmetric tilt grain

boundaries in Y2O3-doped ZrO2. J. Mater. Sci. 46, 4176–4190. (doi:10.1007/s10853-011-5352-8)

68. Lei Y, Ito Y, BrowningND, Mazanec TJ. 2002 Segregation effects at grain boundaries in fluorite

structured ceramics. J. Am. Ceram. Soc. 85, 2359–2363. (doi:10.1111/jace.2002.85.issue-9)

69. McKenna K, Shluger A. 2009 The interaction of oxygen vacancies with grain boundaries in

monoclinic HfO2. Appl. Phys. Lett. 95, 222111. (doi:10.1063/1.3271184)

70. Lee W, Jung HJ, Lee MH, Kim YB, Park JS, Sinclair R, Prinz FB. 2012 Oxygen surface

exchange at grain boundaries of oxide ion conductors. Adv. Funct. Mater. 22, 965–971.

(doi:10.1002/adfm.v22.5)

71. Chiang YM, Lavik EB, Blom DA. 1997 Defect thermodynamics and electrical properties of

nanocrystalline oxides: pure and doped CeO2. Nanostruct. Mater. 9, 633–642. (doi:10.1016/

S0965-9773(97)00142-6)

72. Matzke H. 1987 Atomic transport properties in UO2 and mixed oxides (U, Pu)O2. J. Chem.

Soc., Faraday Trans. 2 83, 1121–1142. (doi:10.1039/f29878301121)

73. Palheiros F, Gonzaga R, Soares A. 2009 Comparative study of the different industrial

manufacturing routes for UO2 pellet specifications through the wet process. In ICAM - Int.

Conf. on Advanced Materials, 2009. Q5

74. Guo H, Tian C, Wang X, Lv N, Ma M, Wei Y. 2016 Decay chain deduction of uranium fission

products. Health Phys. 1, 17–21. (doi:10.1097/HP.0000000000000521)

75. Chernia Z, Eliyahu Y, Kimmel G, Braun G, Sariel J. 2006 The initial stage of uranium oxidation:

mechanism of UO2 scale formation in the presence of a native lateral stress field. J. Phys. Chem.

B 110, 23041. (doi:10.1021/jp062795n)

76. Symington AR. 2018 symmy596/PolyPy: Version 0.2.2. (doi.org/10.5281/zenodo.2271509)